On the formation of the lunar herringbone pattern

VERNE R. OBERBECK and ROBERT H. MORRISON

NASA-Ames Research Center, Moffett Field, California 94035

Abstract—The V-shaped ridge components of the lunar herringbone pattern are simulated by simultaneous and nearly simultaneous impact cratering in the laboratory. The results of the simulations, together with a mathematical model developed for the case of simultaneous impacts, indicate that the pattern resulted from simultaneous impact formation of adjacent secondary craters. In addition, preliminary experimental results suggest that many secondaries of the crater Copernicus were produced by fragments that impacted either simultaneously or nearly simultaneously with the uprange fragments impacting first, at angles greater than 60° measured from the normal to the surface.

INTRODUCTION

THE LUNAR herringbone pattern consists of groups of V-shaped ridges. It is a common lunar surface feature typically associated with the secondary craters that surround many large craters. O'Keefe *et al.* (1969) first described these features and hypothesized that they were caused by erosion due to a hypersonic gas flow associated with a hypothetical base surge from the primary crater. Subsequently, Guest and Murray (1971) also described these features and concluded that they were mainly due to a depositional mechanism. Schultz (1972) also noted the association of the herringbone pattern ridges with secondary craters and suggested that they were produced as a result of the interaction of gases and molten material ejected from the primary crater with material ejected from the secondary crater. Based on laboratory impact cratering studies, Oberbeck *et al.* (1972) and Oberbeck and Morrison (1973) provided evidence that the herringbone pattern's ridge components are deposits of ejecta resulting from collision of material ejected from closely spaced secondary impact craters formed nearly simultaneously. The laboratory evidence, coupled with an observed association of herringbone ridge components with secondary craters, provides a method for determining the impact origin of secondary craters and the conditions for their formation.

The present paper presents examples of lunar herringbone ridge components associated only with nearly tangential members of crater chains, and additional experimental results of simulation of these features. A mathematical model describing the mechanism of formation of these features is also presented. Results of the paper then are applied to interpretation of the origin of the Davy Crater chain.

NATURE OF THE HERRINGBONE PATTERN AND DISTRIBUTION OF LUNAR SECONDARY CRATERS

Lunar secondary craters occur as isolated craters and in arcuate loops and linear chains of overlapping craters. Some are markedly elongate in shape and shallower in depth compared to most other small lunar craters, and typically there is no visible rim or only a very low rim (Shoemaker, 1962). They occur within the high-albedo diffuse elements of the rays and, for the crater Copernicus, are often at the ends of ray elements nearest Copernicus (Shoemaker, 1962). They are probably the source of much of the debris that formed myriads of small lunar concentric craters which are believed to be the cause of the bright ray segments associated with many lunar secondary craters (Oberbeck, 1971).

Figure 1 shows a photomosaic of Copernicus, a good example of a lunar rayed crater with fresh secondary craters. Long strings and loops of craters and repeating clusters of craters are visible in this photomosaic. A large loop of secondary craters is directed to the southeast of Copernicus toward the crater Mösting. Also, another much smaller arcuate chain of craters exists between Copernicus and the crater Reinhold. However, most craters occur in crater chains nearly radial to Copernicus. An example is the string of craters due north of Copernicus. Some
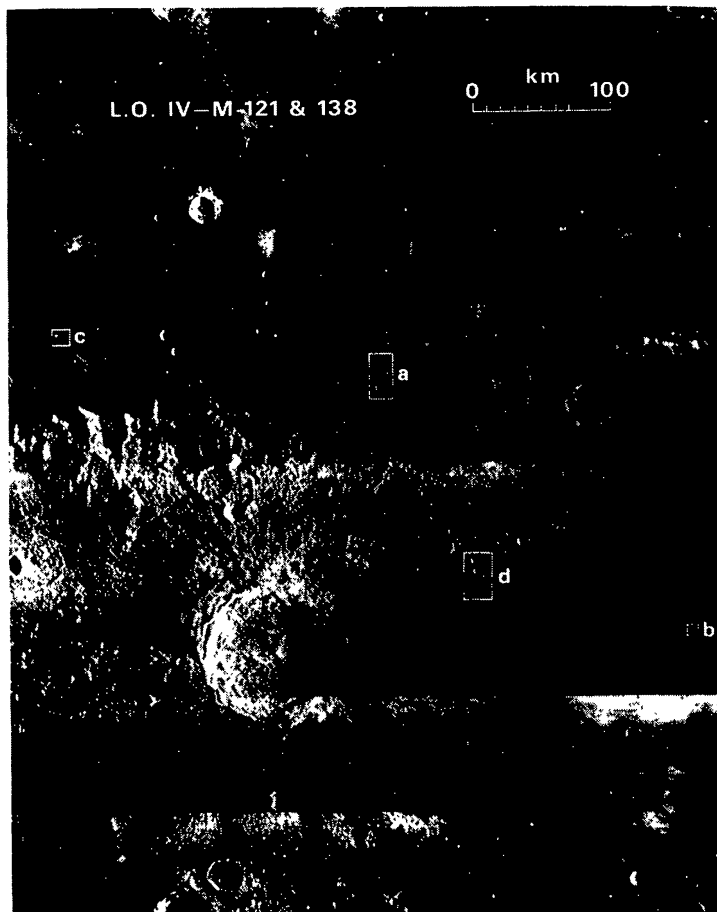

Fig. 1. Photomosaic of lunar crater Copernicus and four crater chains shown in Fig. 2.

crater chains lie at angles to lines radial from the center of Copernicus, such as the well-defined chain of secondaries midway between Copernicus and the crater Eratosthenes. This chain consists of three segments of overlapping craters in the part of the chain striking northwestward and a northerly segment that extends to a point approximately 350 km from the center of Copernicus. Part of this segment is shown in Fig. 2a. O'Keefe *et al.* (1969) used this as an example of the herringbone pattern. They noted that the typical lineations of the herringbone pattern formed approximately equal angles to the radial line from the center of the crater and that in some regions the lineations were visible as appendages to craters, especially where the craters occur in lines as in Fig. 2a. Guest and Murray (1971) have described the herringbone pattern around Copernicus, and they showed that components of the herringbone patterns are V-shaped ridges. Figures 2b, c, and d
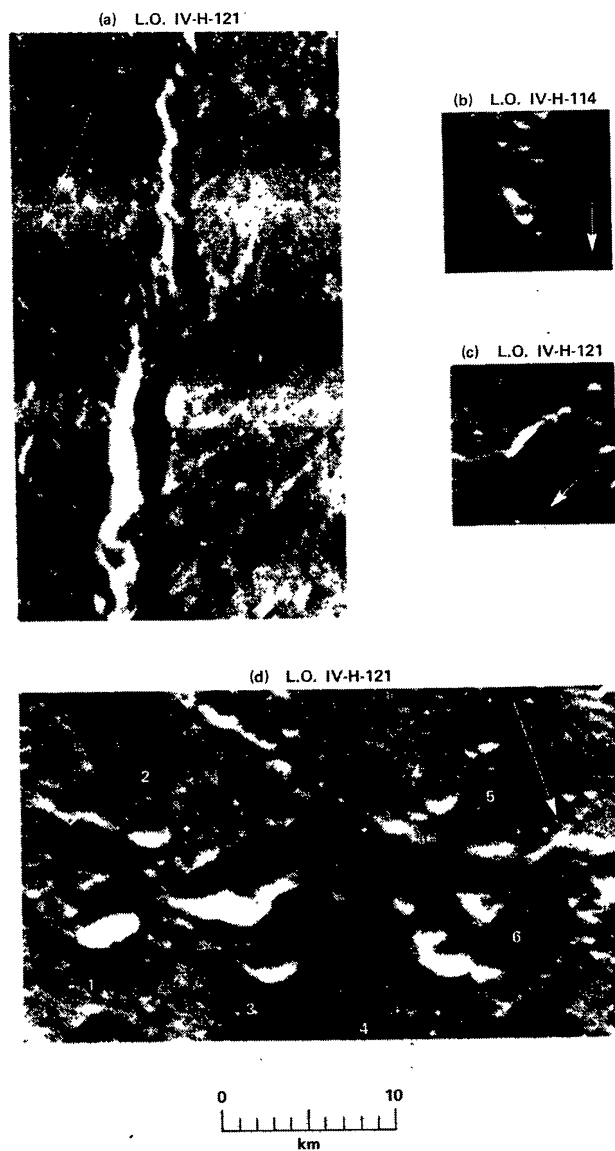

Fig. 2. Four secondary crater chains of Copernicus.

show additional crater chains keyed to the photomosaic of Fig. 1 to show their locations with respect to Copernicus. Crater chains (b) and (c) have subdued ridges projecting from the points of intersection of the crater rims. More well-developed ridges are associated with the secondary craters shown in Fig. 2d. The arrow on this photograph points to the center of Copernicus, and its direction corresponds to the axes of symmetry of the V-shaped ridges. Lunar secondary craters are not always characterized by full V-shaped ridges. Figure 3 shows part of an Apollo metric camera photograph and magnified views of three crater chains. (The direction to Copernicus is toward the bottom of the figure.) Crater chains (b) and (c) are considered to be secondaries of Copernicus since they occur on a well-developed Copernican ray. They have axes offset from the radial line to the center of Copernicus with ridges existing on only one side.

Other large lunar craters have secondary craters with V-shaped ridges. The crater Timocharis is shown on metric camera frame 598 of Fig. 4. Although its ejecta blanket has been eroded by subsequent impacts, many small secondary craters with good examples of subdued herringbone patterns are visible. Crater chains (a) and (d) are subdued examples containing craters about 1 km in diameter. The magnifications reveal V-shaped ridges that point towards Timocharis. Crater doublets (b) and (c) each have ridges between the craters, suggesting that
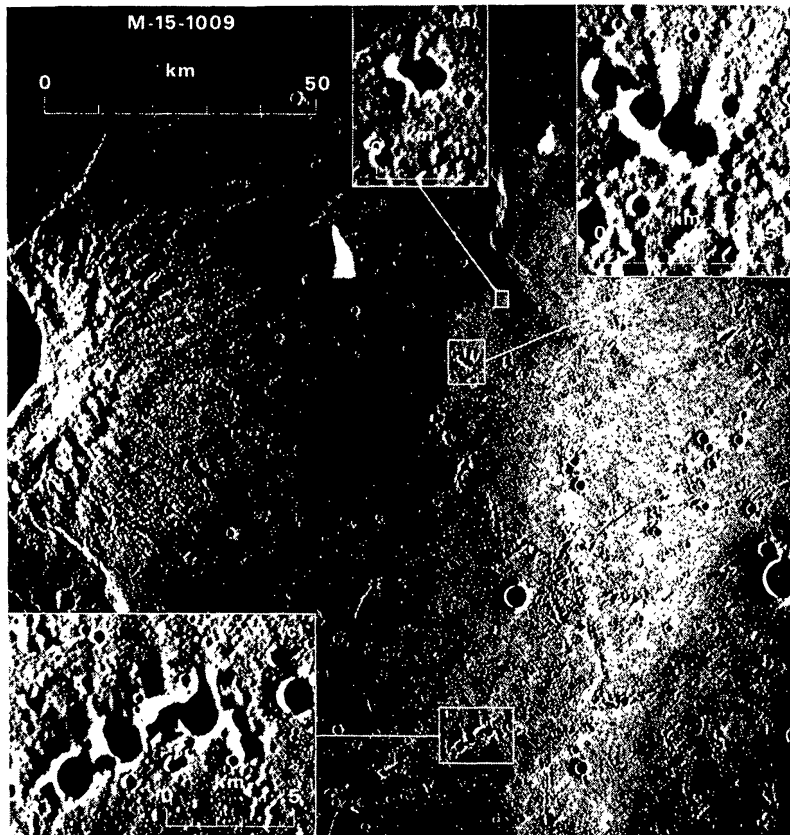

Fig. 3. Part of Apollo 15 metric frame 1009 showing lunar surface area north of Copernicus and V-shaped ridges associated with Copernican secondary craters.
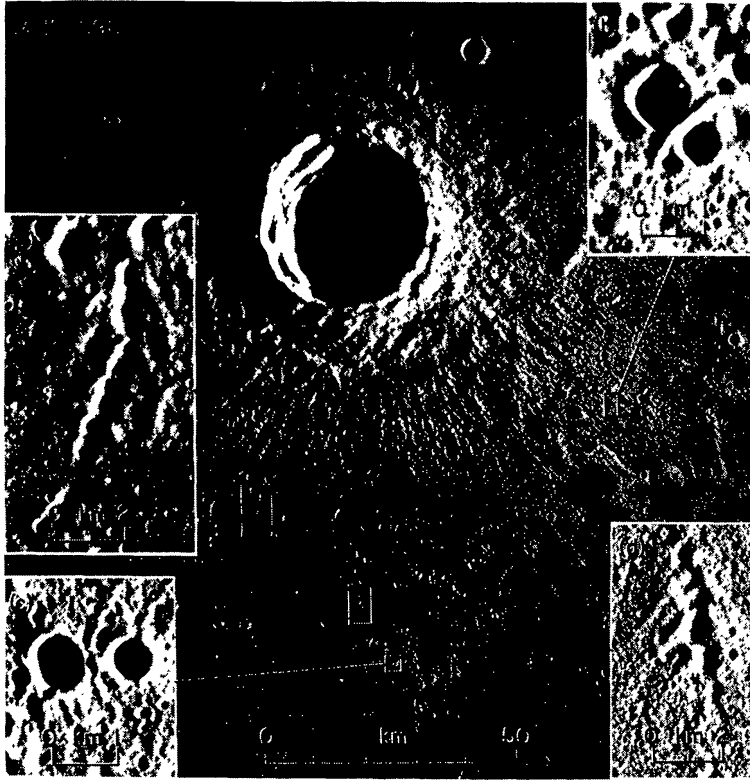
Fig. 4. Apollo 15 metric photograph 598 showing the crater Timocharis, two secondary chains of Timocharis (a, d) and two crater pairs produced by simultaneous impact of debris ejected from another primary crater.

they were produced by simultaneous impact. However, these are probably secondary craters of a different lunar primary crater because photographs taken under other conditions of lunar lighting show that they are much fresher than other secondary craters of Timocharis. Thus, some secondary crater fields of certain lunar craters probably contain secondaries of other craters.

Figure 5 shows an Apollo photograph of the crater Euler. The eastern half of the secondary crater field contains ridge elements associated with rather uniformly distributed secondary craters. They produce a general appearance of a subdued herringbone pattern. The larger crater chains magnified in this figure are believed to be associated with other craters. Crater chain (a) near Euler has an associated herringbone pattern. Because the crater chain's axis of symmetry is tangential to Euler, it could be argued that the secondaries were produced from throwout of material from Euler. However, they are probably not secondaries of Euler because these craters are much larger than the other secondaries. The other two crater groups shown in this figure are believed to be secondary craters of Copernicus because they occur on well-developed Copernican rays. The groups also are characterized by V-shaped ridges pointing towards Copernicus that give a herringbone-pattern appearance. The included angle of the Vs is approximately 70–90° for these examples. Other secondary craters of Copernicus are shown in Fig. 6. The Apollo 17 metric photograph shows the lunar surface area southeast of
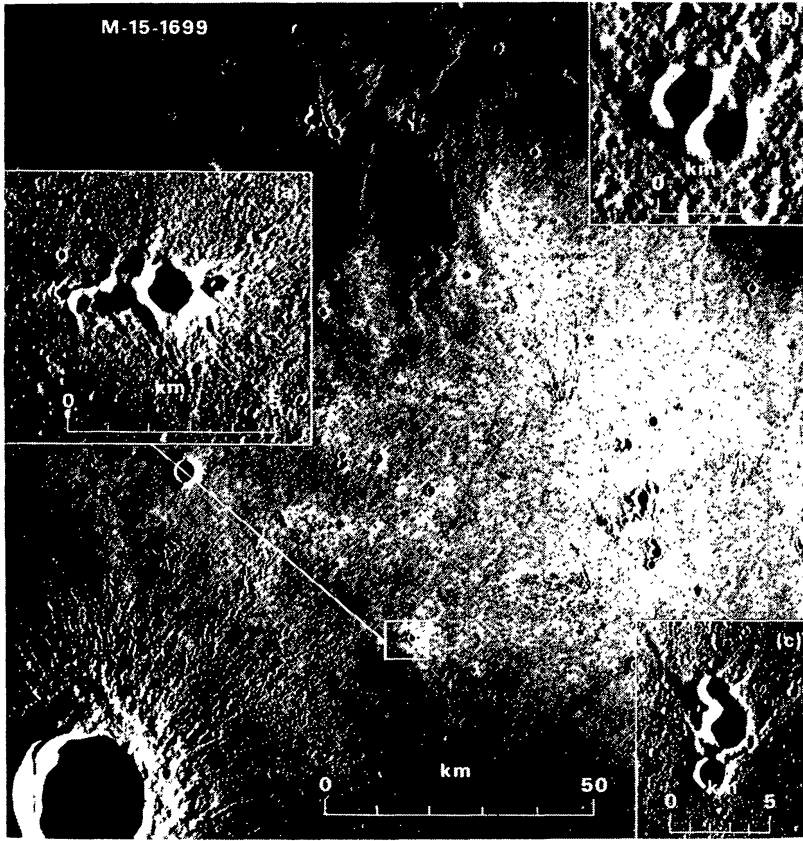
M-15-1699

Fig. 5. Apollo 15 metric photograph 1699 showing the crater Euler and secondary crater chains of Aristarcus (?) and Copernicus and the associated V-shaped ridges.
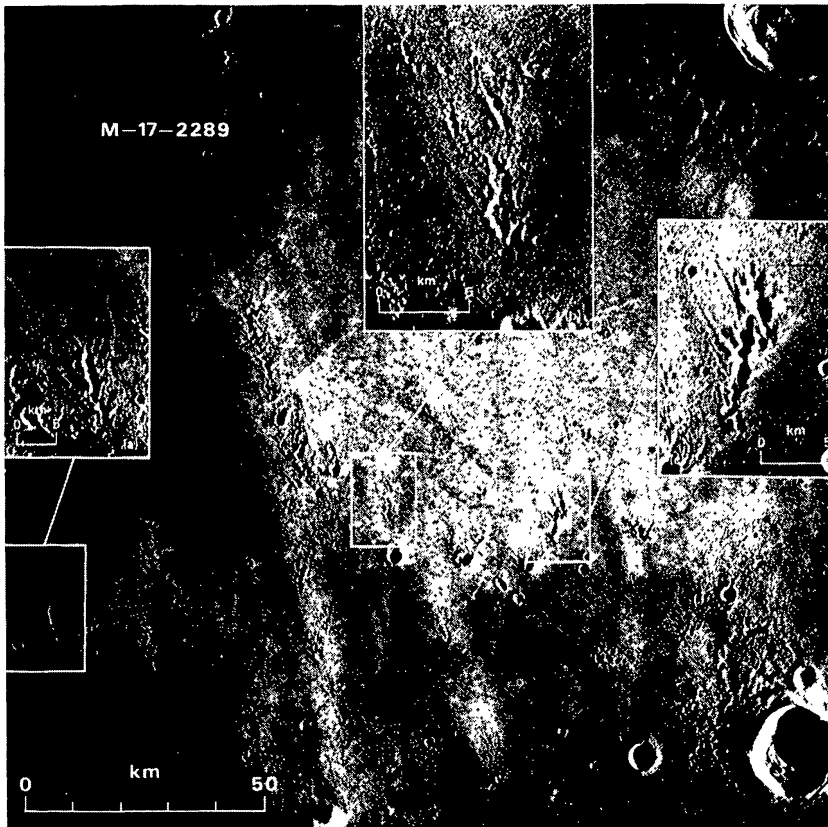
M—17—2289

Fig. 6. Apollo 17 metric photograph 2289 showing secondary crater chains of Copernicus Crater and associated V-shaped ridges.

112

the area shown in Fig. 5. Crater chain (c) of Fig. 5 appears in the upper left of Fig. 6. Three crater chains are magnified in Fig. 6 and all have V-shaped ridges pointing to the south towards Copernicus. The ridges are very well developed on chain (b) where the included ridge angle is about 60°.

In summary, Lunar Orbiter and Apollo photographs show that many secondary craters possess ridges radiating either from nearly circular craters or from crater chains. Usually, the ridge projects to both sides of the crater or crater group, and when this occurs the ridges form a V that points towards the source crater. Included angles of the ridges range from 60 to 130°. However, occasionally the axis of symmetry of the secondary crater chain is not radial to the parent crater. Where this occurs, the ridge may be well developed on only one side of the secondary craters.

IMPACT SIMULATION OF THE HERRINGBONE PATTERN

The most common hypothesis for the formation of secondary craters is that they were produced by impact of material ejected from primary craters. If so, much of the debris would have impacted the surface nearly simultaneously. Therefore, the herringbone ridge components may result from nearly simultaneous formation of adjacent impact craters.

Preliminary results of simulation of the herringbone pattern's ridge elements by simultaneous impact of two projectiles against quartz sand targets have been presented by Oberbeck *et al.* (1972) and Oberbeck and Morrison (1973). Their papers describe the experimental techniques and determination of the conditions of simulation of lunar secondaries. From these simulations, they found that the ridges typically associated with tangential craters were nearly perpendicular to the crater pairs' axes of symmetry. Only for impact at very high angles to the surface normal were craters produced with V-shaped ridges resembling lunar herringbone ridge components. However, these simulations were performed only by impacting simultaneously two projectiles separated at a distance of approximately one crater diameter.

Additional experiments now have been performed under other impact conditions. Because secondary fragments probably impacted at slightly different times, the relative times of impact of the two projectiles were varied in the new tests. Figure 7 illustrates such crater pairs produced by simultaneous impact, by impact of a projectile uprange first (positive τ), and by impact of a projectile downrange first (negative τ) at each of two impact angles, 30° and 82.5°. Average impact velocities at the two angles were 0.6 and 0.8 km/sec, respectively. These conditions are near the midpoints of the ballistic curves of Fig. 8, which define the necessary conditions (Oberbeck and Morrison, 1973) required to simulate typical lunar secondary craters formed at ranges from 100 to 400 km from the primary crater, assuming that they are produced by impact of material ejected from the primary crater. For each impact angle, the included angle of the ridge, measured on the downrange side, decreases as τ increases. The best examples of V-shaped ridges point uprange and are formed when the crater uprange is produced first. For example, the included angle of the ridge structure is only about 90° when the
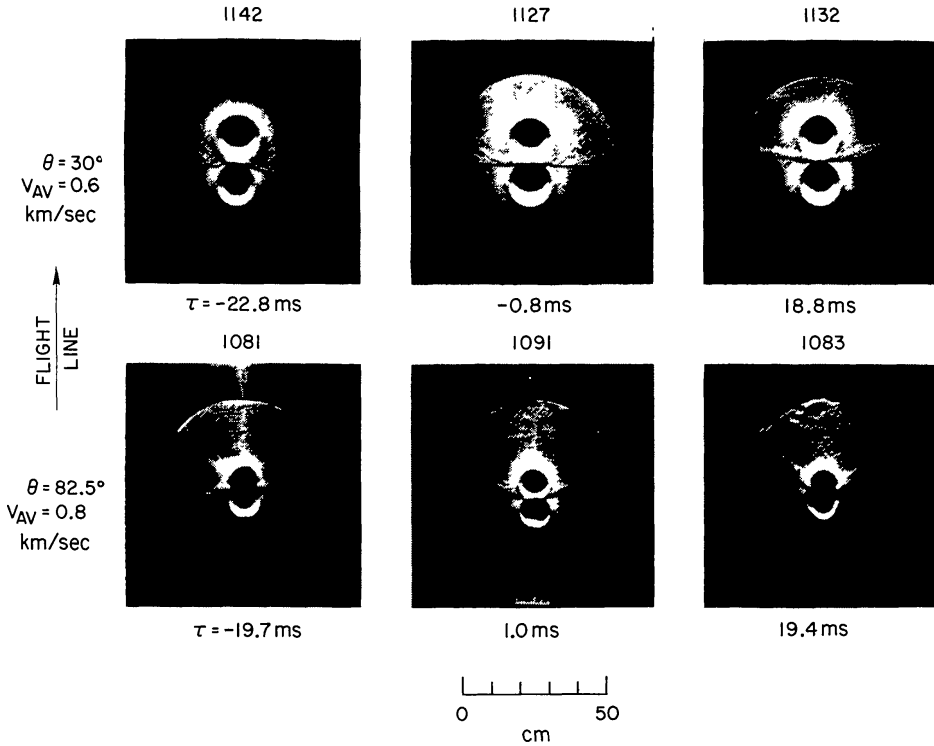
Fig. 7. Crater pairs produced by impact of two projectiles at 30° and 82.5°. Relative time of impact, τ, is varied for each impact angle.

impact angle is 82.5° and the uprange projectile impacts 19.4 ms. before the down-range projectile. This is well within the range of values measured for lunar her-ringbone ridge components by Guest and Murray (1971) and reported by Ober-beck and Morrison (1973). It is noteworthy that when the impact angle is 30° and the downrange projectile impacts 22.8 ms. before the uprange projectile, the V
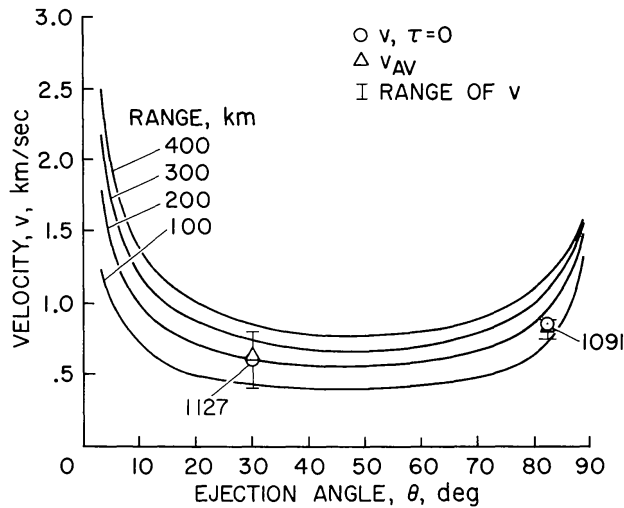

Fig. 8. Conditions of ejection velocity and angle required to propel material to ranges from 100 to 400 km from primary craters.

actually points downrange (experiment 1142). The fact that such lunar herring-bone ridge components have not been found is consistent with the fact that impact should occur first for craters nearest the primary craters.

High speed motion picture records have been used by Oberbeck and Morrison (1973) to show that the ridges formed near crater pairs produced by simultaneous impact result from collision of material ejected from both craters. Such records also may be used to explain the dependence of the included angle of the V-shaped ridges on the relative time of impact. Figures 9a and b illustrate frames selected from high speed movie records of the impacts that produced the craters of Fig. 7. Three different times (10, 50, and 100 ms. after impact of the second projectile) during growth of each crater pair are illustrated. Most of the photographs exhibit well-developed concentrations of ejecta in the middle of the combined ejecta plumes. This represents a zone of collision of material ejected from both craters. Moreover, there is a definite relationship between the change in the angle of these collision zones with relative time of impact and the change in included angle of the V-shaped ridge with relative time of impact. For example, Fig. 9a shows that when the impact angle is 30° the collision zone becomes more inclined downrange as τ increases. This corresponds to a decrease in included angle of the ridge as τ increases (*see* Fig. 7). Similarly, the photographs of Fig. 9b can be related to the photographs of craters in Fig. 7, but high speed movie records for $\tau = 19.4$ ms. do not clearly show the collision zone.

Guest and Murray (1971) have noted that most lunar secondary chains are radial to the parent craters, and this is consistent with our findings. Thus, the experimental simulation results can be applied to interpretation of the conditions of formation of lunar secondary craters if laboratory crater pairs are compared to lunar crater pairs where members of the chain are equal in size and for which the axes of symmetry are radial to the source crater.

Most secondary carter chains illustrated in this paper occur along lines nearly radial to the primary craters. The included angle of the V-shaped herringbone components associated with these craters varies from about 60 to 130°. The pre-liminary experimental results suggest that such V-shaped ridges are produced only when projectiles impact at angles greater than 60°, measured from the surface normal.

Model of Ridge Formation Associated with Simultaneous Impacts

Some insight into the mechanism for the formation of a ridge that projects from two adjacent secondary craters is provided by an idealized model developed for a simple case where impacts are simultaneous and normal to the target surface. Because the ejecta plumes in this case are symmetric, their interaction is much simpler than that of the oblique impacts shown in Fig. 9. This can be seen in Fig. 10 which shows nine high speed movie frames for the simultaneous, normal impact case. The impact velocity is 2.3 km/sec. Unlike the oblique impact case, the particles ejected from each crater collide along a vertical plane midway between the craters. This is evident from the cloud of particles midway between the

$\theta = 30°$ v = 0.53 TO 0.61 km/sec

0   50
cm

$\tau =$
−22.8 ms

$\tau =$
−0.8 ms

$\tau =$
18.8 ms

t = 10 ms   t = 50 ms   t = 100 ms

(a)

$\theta = 82.5°$ v = 0.76 TO 0.86 km/sec

0   50
cm

$\tau =$
−19.7 ms

$\tau =$
1.0 ms

$\tau =$
19.4 ms

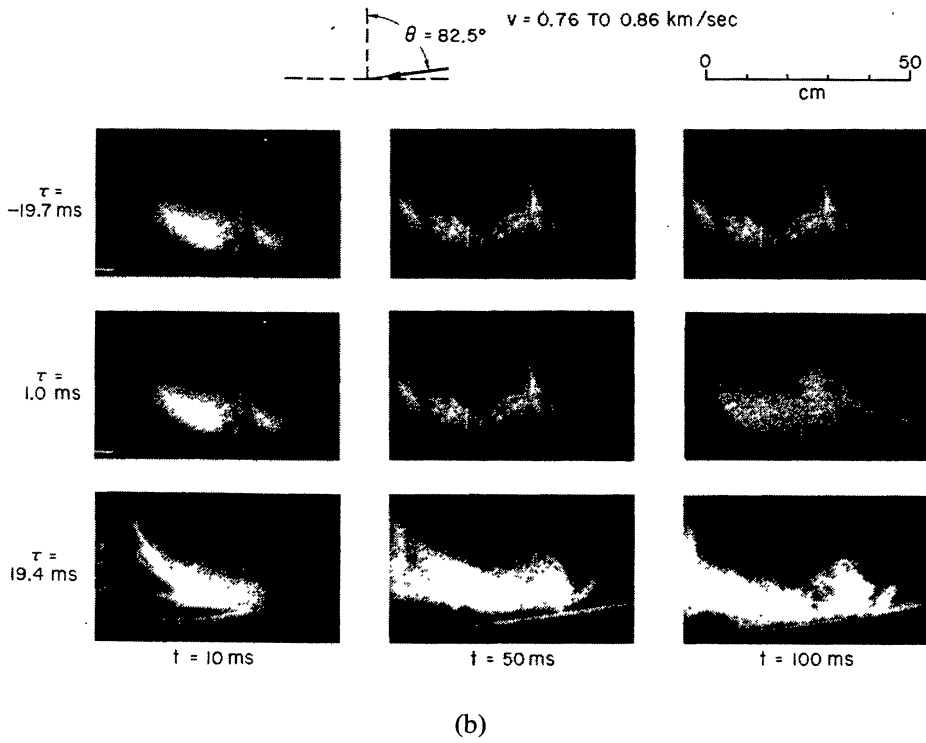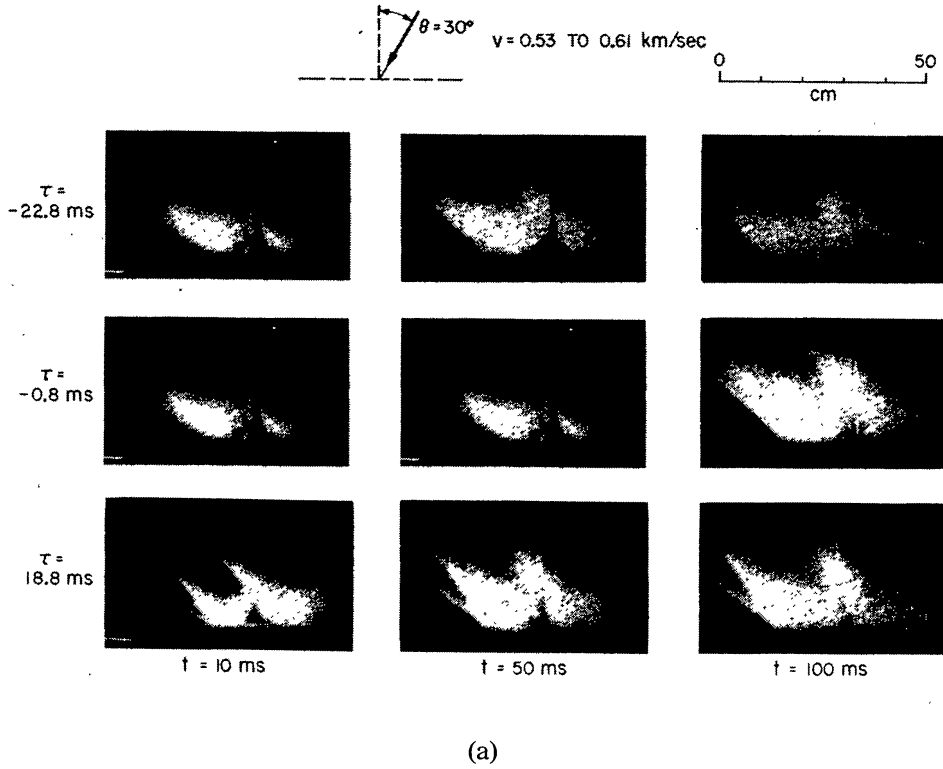t = 10 ms   t = 50 ms   t = 100 ms

(b)

Fig. 9. Frames from high speed motion picture records of three stages in crater pair growth 10, 50, and 100 ms. for craters formed by projectiles impacting at different times, τ, for (a) 30° impact angle and (b) 82.5° impact angle.
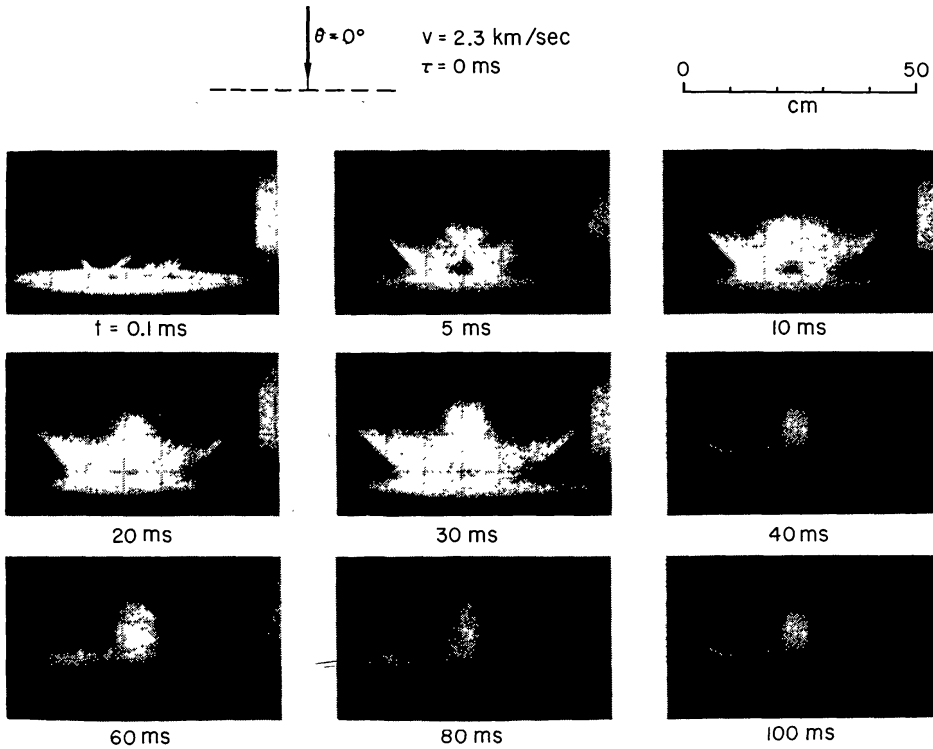
Fig. 10. Selected frames of high speed motion picture record of simultaneous, normal impact of two projectiles.

craters that first becomes discernible at 20 ms. after impact and grows until 100 ms. after impact where it is the dominant feature. A cloud results from the collision of the particles because the collisions are not perfectly plastic, thus causing the particles to rebound slightly with small velocity components parallel to the crater pair's bilateral axis of symmetry. Thus, the collision products are in trajectories at low angles to the plane perpendicular to the bilateral axis.

The impact case of Fig. 10 is idealized in Fig. 11, which shows two craters separated by distance S, each with a diameter D_i, forming in the target at time t'. The coordinate system is fixed in the target with the origin midway between the craters; the X-axis is coincident with the bilateral axis of symmetry; and the Z-axis is normal to the target surface. In this idealization, it is assumed that all the particles that are ejected from both craters toward one another collide, even though this is not strictly true for times less than 30 ms. after impact (see Fig. 10). Consider, therefore, two particles, a and b, ejected at time t' at identical trajectory angles and velocities from points A and B, respectively, each point being the point of intersection of the crater rim by a line from the crater's center at an angle λ to the X-axis. If $-\lambda_{cr} \le \lambda \le \lambda_{cr}$, where λ_{cr} is a critical angle (to be defined later), the particles collide at point C midway between the craters and after rebounding fall back to impact the surface at points E and F. If $\lambda_{cr} < \lambda < 2\pi - \lambda_{cr}$, the particles do not collide, but impact the target surface individually.
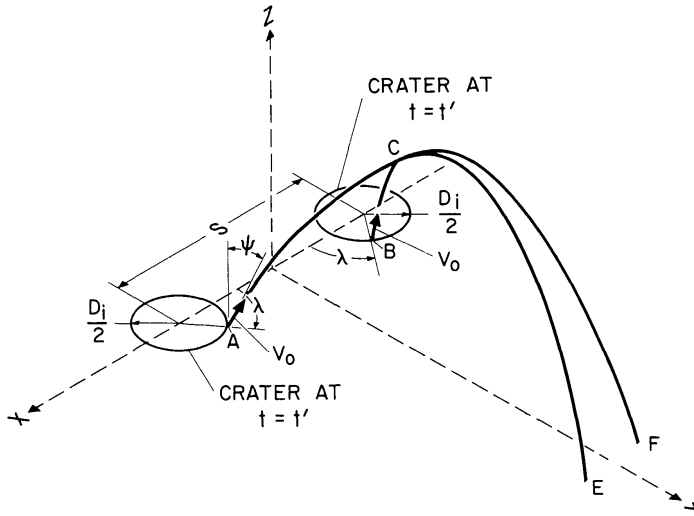
Fig. 11. Schematic for calculation of the trajectories and final impact points of material ejected from the rims of two craters produced simultaneously by projectiles impacting the target normal to the surface.

The equations of motion for the two particles are

$$d^2X_a/dT^2 = d^2X_b/dT^2 = 0, \tag{1a}$$

$$d^2Y_a/dT^2 = d^2Y_b/dT^2 = 0, \tag{1b}$$

and

$$d^2Z_a/dT^2 = d^2Z_b/dT^2 = -g, \tag{1c}$$

where $T \equiv t - t'$ and g is the acceleration due to gravity. Integrating Eqs. (1) twice and evaluating the constants at $T = 0$ yield the following equations for the particles' trajectories for times up to collision or impact with the surface, as the case may be:

$$X_a = -X_b = -(V_0T \sin \psi + D_i/2) \cos \lambda + S/2; \tag{2a}$$

$$Y_a = Y_b = (V_0T \sin \psi + D_i/2) \sin \lambda; \tag{2b}$$

$$Z_a = Z_b = -gT^2/2 + V_oT \cos \psi. \tag{2c}$$

Here, $V_0 = V_0(t')$ and $\psi = \psi(t')$ are the velocity and the angle with respect to the normal to the surface at which the particles are ejected.

In the case where particles a and b collide at point C, one may determine the particles' trajectories for times after collision up to impact with the surface in the following manner. Since it follows from considerations of symmetry that the collision causes a change only in the X-components of the particles' velocities, the Y- and Z-components of the particles' trajectories are still given by Eqs. (2b) and (2c). The X-components, however, are found from the conservation of momentum equation and the equation defining the coefficient of restitution. If one assumes that the particles' masses are the same, these equations are

$$V'_{xa} + V'_{xb} = V_{xa} + V_{xb} \tag{3}$$

and

$$V'_{xa} - V'_{xb} = -\epsilon(V_{xa} - V_{xb}), \tag{4}$$

respectively, where ϵ is the coefficient of restitution and V_x and V'_x are the X-components of velocity just before and just after collision, respectively. Combining Eqs. (3) and (4) yields

$$V'_{xa} = [(1-\epsilon)V_{xa} + (1+\epsilon)V_{xb}]/2 \tag{5a}$$

and

$$V'_{xb} = [(1+\epsilon)V_{xa} + (1-\epsilon)V_{xb}]/2. \tag{5b}$$

Substituting into Eq. (5) the relations obtained for V_{xa} and V_{xb} by differentiating Eq. (2a) gives

$$V'_{xa} = -V'_{xb} = \epsilon V_0 \sin \psi \cos \lambda,$$

or

$$dX_a/dT = -dX_b/dT = \epsilon V_0 \sin \psi \cos \lambda. \tag{6}$$

Integrating Eq. (6) and evaluating the constant at the time of collision yield the following equation for the X-components of the particles' trajectories:

$$X_a = -X_b = \epsilon[(V_0 T \sin \psi + D_i/2) \cos \lambda - S/2]. \tag{7}$$

At time T_f the particles impact the surface, and

$$Z_a\Big|_{T=T_f} = Z_b\Big|_{T=T_f} = 0.$$

This condition, together with Eq. (2c) provides the following relation for T_f:

$$T_f = 2V_0 \cos \psi/g.$$

Substituting this into Eqs. (2a) and (2b), where $T = T_f$, one obtains equations, in nondimensional form, for the coordinates of points E and F when $\lambda_{cr} < \lambda < 2\pi - \lambda_{cr}$ (that is, the case where the particles do not collide but impact the surface individually). The equations are

$$X_E/D = -X_F/D = -K \cos \lambda + S/(2D), \tag{8a}$$

and

$$Y_E/D = -Y_F/D = K \sin \lambda, \tag{8b}$$

where D is the final crater diameter and K is defined by the equation

$$K = V_0^2 \sin \psi/(Dg) + D_i/(2D). \tag{9}$$

Similarly, from Eqs. (7) and (2b), one obtains the following equations for the coordinates when $-\lambda_{cr} \leq \lambda \leq \lambda_{cr}$ (that is, the case where the particles collide at point C):

$$X_E/D = -X_F/D = \epsilon[K \cos \lambda - S/(2D)], \tag{10a}$$

and

$$Y_E/D = Y_F/D = K \sin \lambda. \tag{10b}$$

And when $\lambda = \lambda_{cr}$, particles a and b collide just as they impact the surface on the Y-axis. Therefore, from Eq. (10a),

$$\cos \lambda_{cr} = S/(2DK),$$

which gives

$$\lambda_{cr} = \text{arc cos } [S/(2DK)]. \tag{11}$$

Before using Eqs. (8) and (10) to calculate the impact points for the particles ejected from the two craters, one must know the relationship for K, which as seen in Eq. (9) depends on the functions of V_0, ψ, and D_i. From measurements of the high speed movie record of Fig. 10, it was possible to determine the following relation for D_i for times 0.1 ms. $\leq t' \leq 40$ ms.:

$$D_i/D = 1 - 0.715 e^{-0.0492t'},$$

where $D = 18.6$ cm.

However, insufficient resolution of the sand particles prevented measurements of V_0 and ψ over long time intervals, and only the values $V_0(1) = 1300$ cm/sec and $\psi(1) = 40°$ (at $t' = 1$ ms.) were measured. Assuming for purposes of computation that V_0 decays exponentially and that $V_0 = 0.001\ V(1)$ when $D_i/D = 0.999$, one obtains the following function for V_0:

$$V_0(t') = 1369 e^{-0.0521t'}.$$

Assuming further that ψ is constant with time one obtains the following relation for K:

$$K = 101.2 e^{-0.1042t'} - 0.3575 e^{-0.0492t'} + 0.5. \tag{12}$$

By assuming arbitrarily that $\epsilon = 0.1$ and by letting $S/D = 1$, Eqs. (8), (10), (11), and (12) were used to calculate the impact points of the particles ejected from each crater for each of the discrete times: $t' = 1$ ms. and $t' = 10, 20, 30, \ldots 100$ ms. (Here it is assumed that the relation for D_i/D applies for times t' up to 100 ms.) For each time, λ was varied from 0 to 2π by equal increments, $\Delta\lambda$. However, $\Delta\lambda$ was changed with time so that the number of points calculated, and subsequently plotted, would be proportional to the number of particles being ejected from the craters at that time.

Figure 12 shows the results of calculations from the model. Here, points are plotted only for the region of the target surface in the vicinity of the craters. The plot shows a concentration of points extending out along the Y-axis from either side of the craters. Although the coefficient of restitution, ϵ, used in the calculations was arbitrarily assumed to be 0.1, larger values of ϵ would result only in a wider simulated ridge, whereas lower values would only make the ridge narrower. Also, the particles that are ejected from both craters toward one another at times less than 30 ms. after impact, which were ignored by the idealized model, do not contribute significantly to the plot of Fig. 12 because of their high velocities and therefore large ranges from the craters. Therefore, the concentration of points in the plot simulates the actual ridge produced by the impact case of Fig. 10 and shown in the photograph of Fig. 12. Thus, results of this model calculation imply
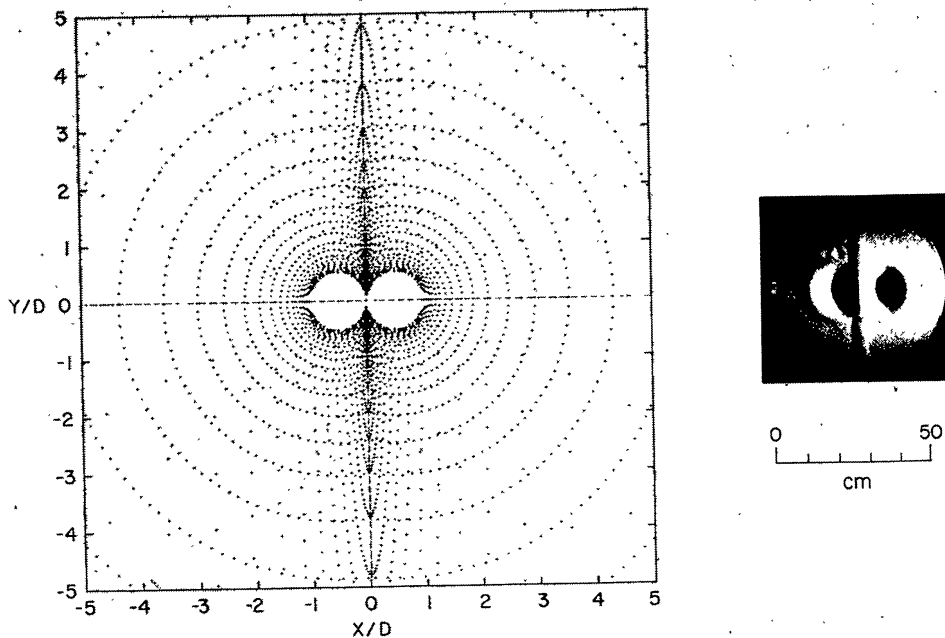
Fig. 12. Calculated impact points of material ejected from rims of two craters produced
by normal impact of two projectiles and photograph of craters being modeled.

that the V-shaped ridge associated with craters produced simultaneously in the
laboratory and those associated with lunar secondary craters are the result of
collision of material ejected from adjacent craters.

Therefore, it is concluded that ridge elements of the lunar herringbone pattern
are natural consequences of simultaneous lunar secondary impact cratering. Their
presence in association with lunar secondary craters is taken as evidence that
lunar secondary craters are in fact produced as a result of the impact of material
ejected from primary craters. Although this interpretation is consistent with the
most common hypothesis for formation of secondaries, it is the first direct evi-
dence that supports that interpretation.

THE DAVY CRATER CHAIN

The lunar herringbone pattern is made up of V-shaped ridge components and,
as has been shown, is typically associated with known lunar secondary craters.
Typically these ridges radiate from between craters and commonly the Vs point
toward the primary crater. However, there are also examples of isolated crater
chains that have ridges nearly perpendicular to the axis of symmetry of the crater
chain and for which there is no apparent source crater. The best example found to
date is the Davy Crater chain.

Figure 13 shows portions of three Apollo 16 metric photographs and one
Apollo 16 panoramic photograph taken under different conditions of sun eleva-
tion. They illustrate the existence of ridges in that part of the crater chain marked
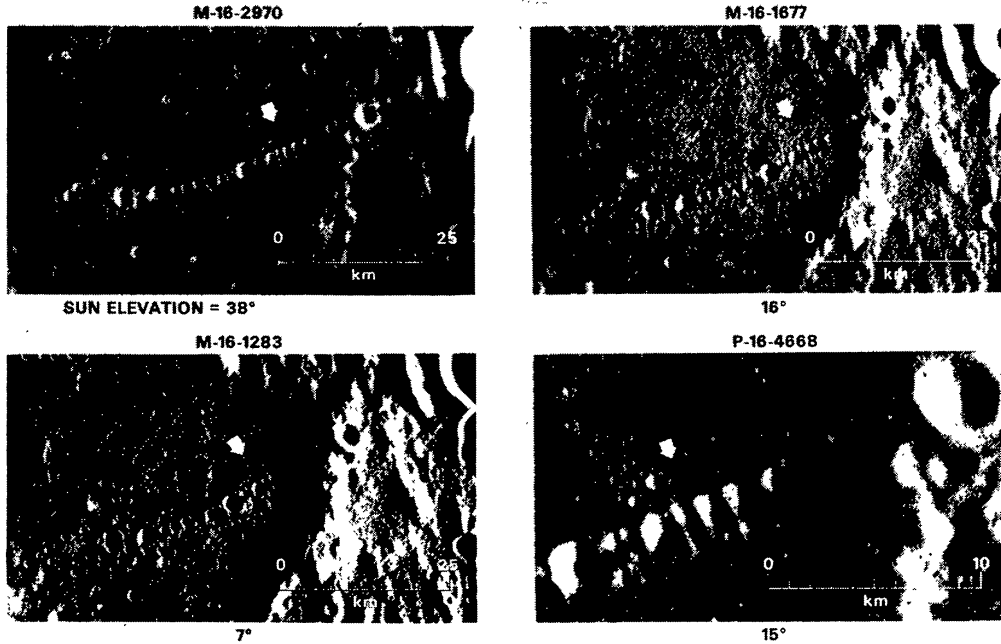
Fig. 13. Parts of Apollo 16 metric and panoramic photographs of the Davy Crater chain.

by the arrow. Inspection of these photographs shows that the ridges are nearly perpendicular to the axis of symmetry of the chain. Their association with those craters closest together is consistent with the impact hypothesis; ridge development is best when impact craters are closely spaced. Also, subdued crater chain members exist on the eastern wall of Davy. This, together with other evidence, suggests that if Davy Crater chain is a string of secondary craters, then the material impacted from the west. Although the source crater has not been located, it is interesting to speculate about such a crater. It need not be very large since most of the craters making up the Davy Crater chain are only about 2 km in diameter, similar in size to many secondaries of Copernicus. Thus, any primary crater comparable in size to Copernicus could have produced the Davy chain. West of Davy Crater chain are many older craters of this size, and any of these are candidates, since Davy chain is not a fresh feature.

Concluding Remarks

The lunar secondary crater herringbone pattern is a result of collision of material ejected from the sites of adjacent impacting fragments. This conclusion is based on successful simulation of ridge components of the herringbone pattern by simultaneous and nearly simultaneous impact cratering in the laboratory, by observations of the growth of such craters, and by mathematical modeling of simultaneous cratering.

Experimental results support the impact hypothesis for formation of lunar secondary craters and provide a means of inferring their conditions of formation. Preliminary results suggest that many secondaries of Copernicus were produced

by fragments that impacted either simultaneously or nearly simultaneously with the uprange fragment impacting first at angles in excess of 60° measured from the normal to the surface. These results are consistent with the findings of Shoemaker (1962), based on a theoretical model for formation of Copernicus; they also imply the existence of a peculiar and as yet unrecognized characteristic of the ballistics of secondary impact cratering. When projectiles impact in the laboratory at high angles to the surface normal, they often ricochet off the target surface, and such conditions of impact for fragments forming secondary craters have been deduced in this study. Therefore, it can be suggested that many secondaries were formed by projectiles impacting at high angles to the surface normal and that these fragments ricocheted and could have produced subdued tertiary craters at greater distances from the secondary craters.

REFERENCES

Guest J. E. and Murray J. B. (1971) A large scale surface pattern associated with the ejecta blanket and rays of Copernicus. *The Moon* **3**, 326–336.

Oberbeck V. R. (1971) A mechanism for the production of lunar crater rays. *The Moon* **2**, 263–278.

Oberbeck V. R., Morrison R. H., and Wedekind J. (1972) Lunar secondary craters. *Apollo 16 Preliminary Science Report*, NASA SP-315, Part K, pp. 29-51 to 29-56.

Oberbeck V. R. and Morrison R. H. (1973) The lunar herringbone pattern. *Apollo 17 Preliminary Science Report*, NASA SP. In press.

O'Keefe J. A., Cameron W. S., and Masursky H. (1969) Hypersonic gas flow in analysis of Apollo 8 photography and visual observations. NASA SP-201, pp. 30–32.

Schultz P. (1972) A preliminary morphologic study of the moon. Ph.D. Thesis, Univ. of Texas at Austin.

Shoemaker E. M. (1962) Interpretation of lunar craters. *Physics and Astronomy of the Moon* (Zdeněk Kopel, ed.) pp. 283–359. Academic Press, New York.